Insights into the enhancement of nanoparticle production throughput by atmospheric-pressure spark ablation

Loizidis, C.; Petallidou, K. C.; Maisser, A.; Bezantakos, S.; Pfeiffer, T. V.; Schmidt-Ott, A.; Biskos, G.

DOI
10.1080/02786826.2024.2403578

Publication date
2024

Document Version
Final published version

Published in
Aerosol Science and Technology

Citation (APA)
Loizidis, C., Petallidou, K. C., Maisser, A., Bezantakos, S., Pfeiffer, T. V., Schmidt-Ott, A., & Biskos, G. (2024). Insights into the enhancement of nanoparticle production throughput by atmospheric-pressure spark ablation. *Aerosol Science and Technology*, *58*(12), 1421-1431. https://doi.org/10.1080/02786826.2024.2403578

Aerosol Science and Technology

ISSN: (Print) (Online) Journal homepage: www.tandfonline.com/journals/uast20

Insights into the enhancement of nanoparticle production throughput by atmospheric-pressure spark ablation

C. Loizidis, K. C. Petallidou, A. Maisser, S. Bezantakos, T. V. Pfeiffer, A. Schmidt-Ott & G. Biskos

To cite this article: C. Loizidis, K. C. Petallidou, A. Maisser, S. Bezantakos, T. V. Pfeiffer, A. Schmidt-Ott & G. Biskos (18 Oct 2024): Insights into the enhancement of nanoparticle production throughput by atmospheric-pressure spark ablation, Aerosol Science and Technology, DOI: 10.1080/02786826.2024.2403578

To link to this article: https://doi.org/10.1080/02786826.2024.2403578

AEROSOL SCIENCE AND TECHNOLOGY
https://doi.org/10.1080/02786826.2024.2403578

Insights into the enhancement of nanoparticle production throughput by atmospheric-pressure spark ablation

C. Loizidis[a], K. C. Petallidou[a], A. Maisser[a], S. Bezantakos[a], T. V. Pfeiffer[b], A. Schmidt-Ott[a,b,c], and G. Biskos[a,d]

[a]Climate and Atmosphere Research Center, The Cyprus Institute, Nicosia, Cyprus; [b]VSParticle B.V, Delft, The Netherlands; [c]Faculty of Applied Sciences, Delft University of Technology, Delft, The Netherlands; [d]Faculty of Civil Engineering and Geosciences, Delft University of Technology, Delft, The Netherlands

ABSTRACT

Spark ablation is a highly effective and versatile method for producing nanoparticles from bulk conductive electrode materials. For a number of applications, however, the production throughput of the process needs to be increased with respect to the current state of the art. Here we show that this can be achieved by decreasing the diameter of the employed bulk-material electrodes from ca. 12 to 0.15 mm, corroborating previous observations, and demonstrate that the throughput is associated with the ablation efficiency (i.e., the energy spent to produce nanoparticles per total input energy) that respectively increases by a factor of 10. It is also shown that the commonly used theory for predicting the mass of nanoparticles produced by spark ablation cannot capture this effect, and thus we extend it to account for heat losses that affect the process when electrode diameter reduces below ca. 2 mm. Through this exercise we also show that reduced heat losses associated with thinner electrodes provide an effective recipe to increase the ablation efficiency, also referred as the nanoparticle production yield. The new extended theory for estimating spark ablation nanoparticle mass production throughput is also accompanied by an empirical equation predicting its dependence on electrode diameter.

GRAPHICAL ABSTRACT

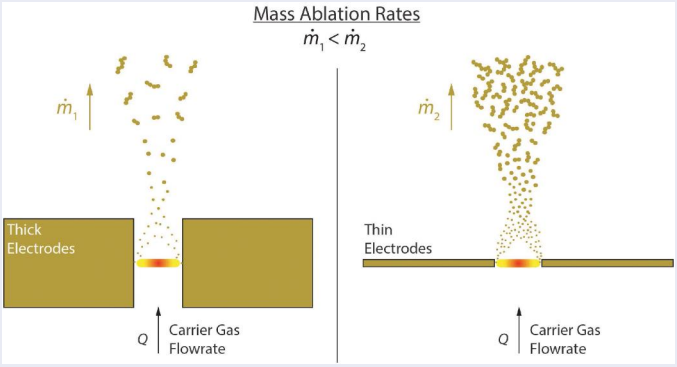

ARTICLE HISTORY
Received 11 April 2024
Accepted 19 August 2024

EDITOR
Jason Olfert

1. Introduction

Spark ablation provides an elegant way of producing tailored nanoparticles. Originally introduced by Schwyn, Garwin, and Schmidt-Ott (1988), the technique has been employed over the years to produce nanoparticles for a number of applications including catalysis (Messing et al. 2010; Lu et al. 2020; Schmidt-Ott 2020) and gas sensing (Isaac et al. 2016, Isaac, Pikaar, and Biskos 2022; Schmidt-Ott 2020), as well as in experiments for understanding fundamentals of nanotoxicity (Gutierrez et al. 2023; Minogiannis et al. 2019) and atomic cluster physics (Maisser et al. 2015, 2021; Schmidt-Ott 2020). Apart

CONTACT G. Biskos g.biskos@cyi.ac.cy, g.biskos@tudelft.nl Faculty of Civil Engineering and Geosciences, Delft University of Technology, Delft, The Netherlands.

Supplemental data for this article can be accessed online at https://doi.org/10.1080/02786826.2024.2403578.

from those applications, the technique is often used to produce test nanoparticles for the characterization and/or the calibration of aerosol instruments (Schmidt-Ott 2020; Zhang et al. 1995).

In a spark-ablation aerosol nanoparticle generator, referred to as Spark Discharge Generator (SDG) from this point onwards, two electrodes are usually placed coaxially next to each other with a small gap between them. In the simplest set-up, periodic electric discharges are induced in this gap through a Resistor Inductor Capacitor (RLC) circuit that is powered by a constant-current/high-voltage source, inducing the discharges in a controllable way and a specific repetition frequency. Each spark is a short-lived hot plasma that has a temperature of 10,000–20,000 K (Kohut et al. 2017), evaporating a small portion of the electrodes each time. The resulting vapor cloud is carried away from the gap region and very rapidly cooled down by a carrier gas flow, forming atomic clusters that rapidly grow to singlet nanoparticles and agglomerated structures by condensation and/or coagulation.

The advantages of the SDG are that: i. it provides a stable source of nanoparticles (Petallidou, Schmidt-Ott, and Biskos 2024), ii. it is highly versatile with respect to the size and composition of nanoparticles it produces (including alloys in a highly controllable manner; Petallidou et al. 2023) and iii. it is environmentally friendly as it does not produce any waste streams (Feng, Biskos, and Schmidt-Ott 2015). Depending on the material used for ablation, the mass throughput (i.e., mass production rate) of existing SDGs typically ranges from ca. 1 to 100 mg/h, which is considered small for many industrial applications. As a result, efforts have been made to increase it by increasing the energy per spark and the repetition frequency (Noh et al. 2017; Feng, Biskos, and Schmidt-Ott 2015; Pfeiffer, Feng, and Schmidt-Ott 2014; Tabrizi et al. 2009), or by using multiple electrode pairs in parallel (Efimov et al. 2013, 2016; Ivanov et al. 2016). We should note here that these measures increase the mass throughput but not the ablation efficiency (also referred to as production yield), defined as the ablation energy, i.e., the energy needed to evaporate material from the electrodes and form nanoparticles, per input energy, i.e., the total energy provided by the SDG electrical circuit.

More than a decade ago, Han et al. (2012) showed that using pin-to-plate or pin-to-rod electrode configurations in spark ablation can lead to higher nanoparticle production throughputs. Along the same lines, Domaschke, Schmidt, and Peukert (2018) provided systematic measurements showing how the throughput of an SDG operated with a constant energy input increases by decreasing the electrode diameter. In addition, they demonstrated how the production throughput for different materials is correlated with the Fourier number that characterizes transient heat transfer. However, this correlation is not general, as the parameters representing the electrode dimensions in the Fourier number predict a decrease of mass production with decreasing electrode diameter, and most importantly does not provide an insightful understanding of the observed effect.

Using a new commercial SDG, here we investigate the dependence of nanoparticle production throughput on the diameter of the employed electrodes, and offer a qualitative theory-based explanation together with a simple semi-empirical model that describes how these two parameters scale. The rest of the paper is organized as follows. Section 2 provides all the details of the experimental setup. Section 3 expands on the state of the art theory for predicting the rate at which material is ablated by electrical sparks, and provides a theoretical framework that captures heat losses and how these vary by changing electrode diameters. Section 4 reports all the experimental and theoretical results, as well as simulations that provide insights of the observed phenomena. Finally, Section 5 summarizes the most important conclusions.

2. Experimental methods

All the experiments reported here were carried out using a SDG manufactured by VS-Particle (VS-Particle, Model G1), with Ni (99.99% purity; Goodfellow GmbH), Cu (>99.95% purity; Goodfellow GmbH) or Pd (99.95% purity; Goodfellow GmbH) electrodes of different diameters. N_2 (99.999% purity) was used as the carrier gas in all cases. The experimental setup and the geometry of the electrodes inside the SDG chamber are shown in Figure 1. In every experiment we used electrodes with different diameters, ranging from 0.15 to 12 mm, while maintaining the other geometric parameters unchanged. In all cases, the shape of the electrodes was cylindrical. The thinner electrodes (i.e., those having diameters <1 mm) were fitted to the SDG holders by extended custom-made adaptors made of stainless steel, in a way that made sure they do not bend during the experiments.

For every electrode pair diameter we measured the mass ablated at different energies per spark, whereas the frequency was kept constant (∼200 ± 20 Hz). The mass ablated from the electrodes was determined gravimetrically by measuring the mass of the electrodes with a high accuracy balance (KERN, Model ABT 100-5 M) before and after running the SDG for a fixed

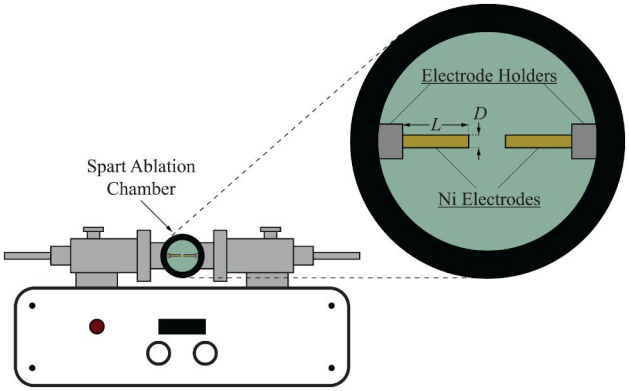

Figure 1. Schematic illustration of the SDG (VS-Particle, Model G1), including details of the configuration of the electrodes, employed in our experiments.

amount of time. The mass ablation yield was estimated by determining the mass ablated per spark as a function of the energy per spark, following the method proposed by Feng, Biskos, and Schmidt-Ott (2015). The production yield of the SDG was subsequently determined by calculating the energy per spark needed to ablate the measured mass (cf. Equation (5) in the next section) and dividing it by the energy provided per spark in the SDG (Feng et al. 2016).

Preliminary gravimetric measurements were carried out in order to exclude that other parameters such as the electrode length, the carrier gas volumetric flow, and its velocity around the electrodes (influenced by the distance between the inlet and the outlet of the SDG), affected the particle mass production (cf. Figure S1 in the online supplementary information [SI]). In addition to these measurements, we carried out systematic tests to ensure that nanoparticle production from the SDG is stable over long periods of time (cf. results in Figures S2 and S3 in the SI). Additional measurements also involved testing the stability of the SDG electric circuit (cf. Figure S4) and determining the mean discharge voltage and sparking frequency of the SDG under the conditions that this was employed (cf. Figure S5). We should note here that the distance between the two electrodes is constantly regulated in the G1 VS-Particle SDG to ca. 1 mm (also confirmed by a caliber with an accuracy of 0.1 mm before and after each experiment) by keeping the discharge voltage and the spark frequency constant during operation. The capacitor employed in this SDG is 20 nF.

3. Theoretical framework

Llewellyn Jones (1950) provided a model, which is still readily used today, relating the mass of material ablated by a single spark discharge with the total input energy of the system. This model can be expressed by the following energy balance:

$$\begin{aligned}\Delta m \cdot \left(C_{ps}(T_m - T) + C_{pl}(T_b - T_m) + H_m + H_e\right) \\ = \alpha E_{tot} - 2\pi r^2 \sigma \tau \left(T_b^4 - T^4\right) - 2\pi r \tau k_{gas}(T_b - T) \\ - 2\pi r \tau k_{elec}(T_b - T)\end{aligned} \quad (1)$$

Starting from the left-hand side of Equation (1), Δm is the mass of electrode material evaporated by each spark, T_m and T_b are the melting and the boiling points of the electrode material, respectively, T is the electrode temperature before the spark (also referred to as the stationary temperature in the rest of the paper), C_{ps} and C_{pl} are the specific heats of the electrode material in the solid and the liquid phase, whereas H_m and H_e are the enthalpies of melting and evaporation of the electrode material, respectively. On the right-hand side of Equation (1), α is the fraction of the total input energy transferred to the electrodes, E_{tot} is the total input energy to the system, σ is the Stefan Boltzmann constant, whereas k_{gas} and k_{elec} are, respectively, the heat conductivity of the gas and of the electrode material. The parameter r is the radius of the spot on which the spark lands (also referred to as the "hot spot"), and τ is the duration of a single spark.

The first term on the left-hand side of Equation (1) represents the energy that goes into ablation, E_{abl}, which is the energy required to evaporate a mass Δm from the electrodes, whereas the terms on the right-hand side account for heat lost: i. *via* radiation, ii. from the electrode to the carrier gas, and iii. from the electrode to the housing of the spark chamber. Considering that, we can collapse Equation (1) to:

$$E_{abl} = \alpha \cdot E_{tot} - E_{EHS}(T), \quad (2)$$

where E_{EHS} represents all the heat loss terms, which are functions of the electrode stationary temperature. In general the ablation energy can be expressed as:

$$E_{abl} = \eta \cdot E_{tot}, \quad (3)$$

where η is the energy efficiency of ablation. To decouple the amount of electrical energy transferred to the electrodes from that lost through heat in the system, we can expand Equation (3) to:

$$E_{abl} = \alpha \cdot E_{tot} - \beta \cdot E_{tot}, \quad (4)$$

where β is the fraction of the total input energy lost as heat. It is reasonable to assume that this loss term is proportional to E_{tot} because the spark diameter is proportional to the spark energy, and thus the fraction of energy, β, transferred to the electrodes is

anticipated to be constant, in contrast to what is assumed to the Llewellyn-Jones approach. We should note here that by combining Equations (3) and (4) yields that $\eta = \alpha - \beta$.

In what follows, we adapt the expression on the left side of the Llewellyn-Jones model (i.e., Equations (1) and (2)) to represent E_{abl}, but replace the electrode heat loss term by $\beta \cdot E_{tot}$, following Equation (4). This leads to:

$$E_{abl} = (\alpha - \beta)\cdot E_{tot} = \Delta m \cdot [C_{ps}(T_m - T) + C_{pl}(T_b - T_m) + H_m + H_e]. \quad (5)$$

We should note here that the Llewellyn-Jones model refers to a single spark event, and this is why it can consider T to be room temperature. In a SDG, multiple sparks follow one another with high repetition, resulting in a considerable warming of the electrodes. As a result, the stationary temperature of the electrodes, T, ranges between room temperature and the electrode melting point considering that the bulk of the electrodes remains solid during the process. Simplifying this process and accounting for electrode heating, our model considers the repetitive sparks (having frequencies that range from 100 to 10,000 Hz for typical SDGs) as a continuous source that heats the face of the electrodes, which consequently forces a temperature gradient along their length.

It is important to note that under conditions leading to a stationary temperature close to the melting point, we expect production of larger micron-sized particles, also referred to as "splashing" particles (Pfeiffer, Feng, and Schmidt-Ott 2014). Splashing, in contrast to evaporation-condensation, is a mechanism by which a liquid pool forms at the hot spot on the electrodes during the sparks, emitting liquid droplets that subsequently cool down to form solid particles in the carrier gas. Qualitative measurements using particles deposited on substrates and observed by electron microscopy did not show any significant variability in the fraction of splashing particles to the rest of the nanoparticles when changing the electrode diameter (data not shown here). As a result, it is reasonable to assume that the production of splashing particles is similar among the different experiments we carried out using electrodes of different diameters for the rest of the analysis.

Expressed now in terms of power, Equations (3) and (4) can be used to estimate the power going into electrode ablation as follows:

$$P_{abl} = \dot{m}\cdot\left[C_{ps}(T_m - T) + C_{pl}(T_b - T_m) + H_m + H_e\right] = \eta \cdot P_{tot} = \alpha \cdot P_{tot} - \beta \cdot P_{tot}, \quad (6)$$

with $\dot{m}$ being the mass production rate. Here, P_{tot} is the total power provided by the SDG power supply, which can be estimated by:

$$P_{tot} = V \cdot I, \quad (7)$$

where I is the constant current charging the capacitor that periodically releases its energy into the spark, and V is the mean voltage across that capacitor. If we neglect electromagnetic losses, P_{tot} is a good estimate for the power required to create the spark discharges.

The second term on the right hand side of Equation (6), (i.e., $\beta \cdot P_{tot}$) is the power lost: i. *via* heat conduction through the solid parts of the SDG, and ii. by forced convection through the carrier gas flow. For the case of a cylindrical rod of length L and diameter D, having a stationary temperature T_{front} at the ablated face and room temperature T_{back} at the other end, this power loss can be expressed as:

$$P_{loss} = \beta \cdot P_{tot} = P_{cond} + P_{conv}, \quad (8)$$

where P_{cond} is the power lost by conduction and P_{conv} by convection (Faghri, Zhang, and Howell 2010), approximated respectively by:

$$P_{cond} = 2 \cdot \frac{k_{elec} \cdot (\pi \cdot D^2)}{4 \cdot L} \cdot \left(T_{front} - T_{back}\right), \quad (9)$$

and

$$P_{conv} = 2 \cdot (\pi \cdot D \cdot L) \cdot U_{conv} \cdot \left(T_s - T_{gas}\right). \quad (10)$$

Here, U_{conv} is the heat transfer coefficient determined by the physical properties of the carrier gas and the shape of the electrodes (cf. Equations (S3)–(S6) in the SI referring to the COMSOL simulations, which are also applicable here). T_{front} and T_{back} in Equation (9) are the mean temperatures of the front edge of the electrodes (i.e., exposed to the sparks) and the back edge of the electrodes (i.e., attached to the SDG holders). In Equation (10), T_s is the mean cylindrical surface temperature of the electrodes (i.e., in contact with the carrier gas flow) and T_{gas} is the temperature of the carrier gas. The factor of 2 in Equations (9) and (10) accounts for the fact that there are two electrodes in the SDG system, assuming that the power is equally distributed between them.

We should note that full consideration of the heat losses (i.e., Equation (8)) should also account for resistive (or Joule) heating caused by the charge carriers transported through the electrodes during the small duration of the repetitive sparks. The power of resistive heating can be estimated as $P_{joule} = I_{d-RMS}^2 \cdot R_{elec}$, where $I_{d\text{-}RMS}$ is the root-mean-square current passing through the electrodes, and R_{elec} their resistance that can be estimated by $\frac{\rho_{elec} \cdot L}{\pi \cdot R^2}$ if

their electrical resistivity, ρ_{elec}, length, L, and radius, R, are known. Calculations of P_{joule} for our system are given in the SI (cf. Section S.8), showing that even for the smallest electrode diameters employed here, Joule heating is negligible compared to P_{cond} and P_{conv}, and can therefore be omitted in the energy balance.

4. Results and discussion

4.1. Evaluation of ablation efficiency

Figure 2a shows how the measured mass ablated per spark Δm, determined by the gravimetric measurements, relates to the total energy per spark E_{tot} for several electrode diameters (cf. also Table S1 of the SI for the values shown in Figure 2a), for Ni electrodes. Evidently, the ablated mass is linearly related to the total energy input, and increases substantially by decreasing electrode diameter from 12 to 0.3 mm (for Ni electrodes). Figure 2b shows the same data as a function of the total energy per spark E_{tot}, but after converting Δm to energy for ablation E_{abl}, according to Equation (5), assuming a stationary temperature of $T = 1013$ K estimated as the mean value between room temperature and the melting point of Ni. The slope of the relation between E_{abl} and E_{tot} provides the energy efficiency of the entire system, η, as indicated by Equation (3). Considering that vapor and particle losses cannot be avoided in the SDG system and in the tubing, estimation of the efficiency using measurements of the mass ablated by the electrodes, as we do here, can be regarded as an upper limit for the particle mass production per unit input energy. Similar results for Cu and Pd electrodes of different diameters (i.e., 2 to 0.15 mm for Cu, and 3 to 0.25 mm for Pd) are provided in the SI (cf. Figures. S6 and S7, as well as Tables S2 and S3).

Figure 3 shows how η varies with the electrode diameter for all the three electrode materials studied in this work. The error bars reflect the minimum and maximum values employed for T, i.e., room temperature and the melting point of the electrode materials, indicating their practically small contribution to ablation efficiency. It is important to note here that the results in Figure 3 agree fairly well with those reported by Domaschke, Schmidt, and Peukert (2018). Although the nanoparticle mass production rate in the two studies was estimated in different ways (i.e., based on gravimetric measurements of the electrodes in our study, and based on mass concentration of the produced particles derived from measurements of the size distributions by Domaschke, Schmidt, and Peukert 2018), the exponents of the fitting curves relating ablation efficiency to electrode diameter were very similar (cf. Figure S8 in the SI).

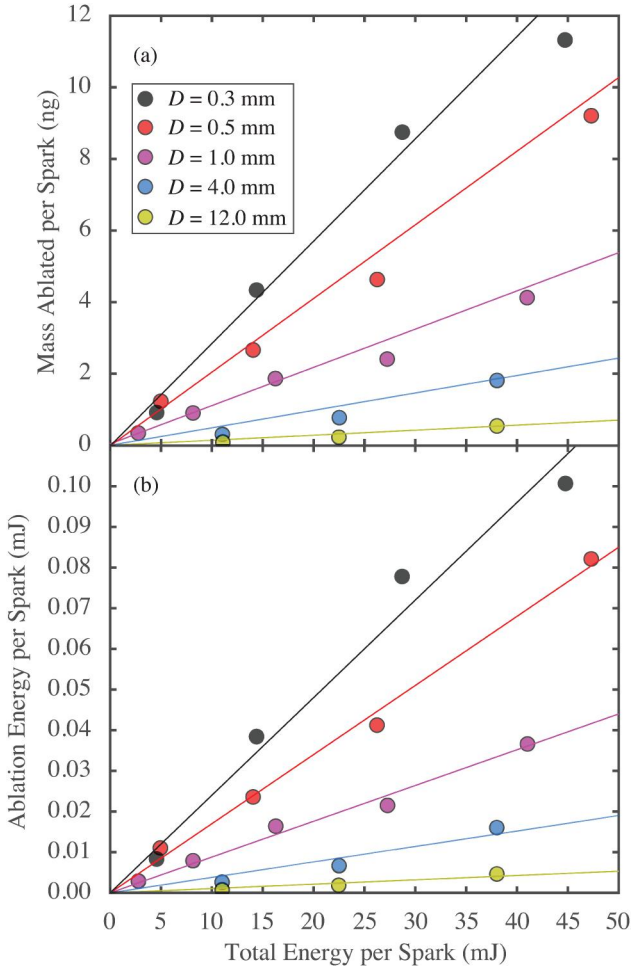

Figure 2. Results from gravimetric measurements corresponding to different diameters of Ni electrodes expressed as: (a) mass ablated from the electrodes as a function of the total electrical energy per spark provided to the SDG, and (b) fraction of input energy going to ablation, determined as the slopes of the fitted curves in the top sub-plot. The flow rate and spark frequency in these measurements were kept constant at 10 L/min N_2 and ~200 ± 20 Hz.

4.2. Estimation of heat losses

Evidently, the ablation efficiency is significantly affected by the diameter of the electrodes, especially as it is reduced below 2 mm, providing the underlying reason for the observed associated increased throughput. However, the question why this happens still remains open. To address this question, we need to quantify the heat losses through the system as indicated by the theory (cf. Equations (9) and (10) in Section 3), for which the face temperature of the electrode is needed. To determine the face temperature we attached a thermocouple to the electrodes as

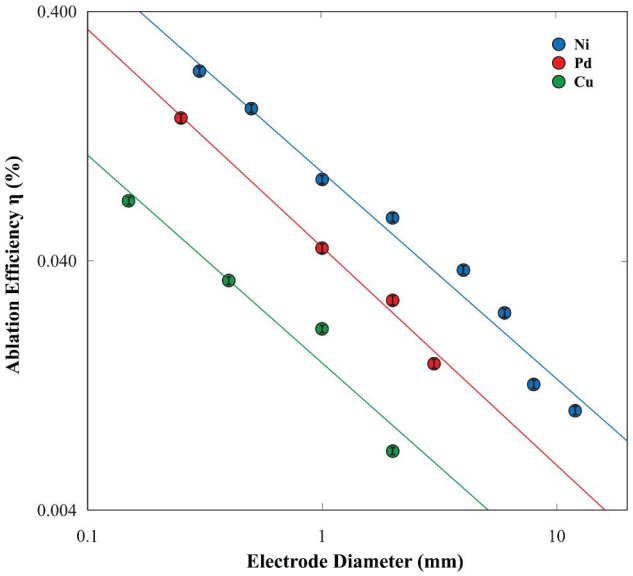

Figure 3. Ablation efficiency, η, as a function of the electrode diameter for the three materials studied in this work. The ablation efficiency is determined by Equation (3), using ablation and total energies determined by the experiments.

discussed and shown in the SI (cf. Section S.5). These measurements show that the equilibrium temperature of the 2- and the 4-mm electrodes are ca. 378 and 352 K, respectively, suggesting that electrodes warm up significantly during the operation of the SDG, and that there are significant associated heat losses.

In order to determine β for any electrode diameter, we use Equations (8)–(10), and an input temperature at the face of the electrode. T_{front} in Equation (9) is assumed to be 378 K, as indicated by the measurements with the thermocouple, T_{back} and T_{gas} are set to room temperature, i.e., 299 K, whereas T_s is assumed to be the average value between T_{front} and T_{back}. Using a value of $L = 27$ mm (which is the length of all the electrodes we employed), we estimate that $P_{loss} \simeq 2$ W for the 2-mm Ni electrodes. Considering that the total input power to the SDG is $P_{tot} \simeq 10$ W yields $\beta = \frac{P_{EHL}}{P_{tot}} \approx 0.2$ for the whole system. Values of the spark ablation efficiencies $\eta = E_{abl}/E_{tot}$ that have been reported so far are around 0.005, indicating that $\eta \ll \beta$. Considering that $\eta = \alpha - \beta$, α and β should have very similar values, and thus the latter gives an estimation of the former, so that $\alpha \approx 0.2$, which is an amazingly high portion of the total energy transferred to the electrodes from the spark plasma. The Llewellyn-Jones model is inconsistent with this result, implying that η is similar to α, or, in other words, that the thermal losses are insignificant.

We must point out that the approximation of β described above is crude due to uncertainties related to the determination of the face temperature of the electrodes. Despite that, however, a safe conclusion we can draw is that heat losses by conduction through the electrode and by convection through the carrier gas, are certainly substantial and that they represent the main energy loss in spark ablation. Our new approach assuming $E_{abl} \propto E_{tot}$, is supported by the results shown in Figure 2b. We cannot describe the heat losses as a small constant value, as the Llewellyn-Jones approach does, but rather as a fraction of the total input energy. This is now captured by our modification of the Llewellyn-Jones model expressed by Equation (6). Given this, the discussion that follows attempts to explain how the electrode diameter can influence the ablation efficiency and consequently the nanoparticle throughput of SDGs.

4.3. Stationary temperature distribution of the whole system

To qualitatively verify the results described in the previous section we carried out finite element calculations, using COMSOL, accounting for the whole temperature profile of the SDG (cf. Section S.6 in the SI). For practical reasons, the successive spark discharges between the two electrodes were considered as a continuous heat source with a power of 20% of the total power provided by the SDG electrical circuit, following the estimation of β described in Section 4.2. The COMSOL simulations consider heat conduction through the electrodes to the housing, forced convection to the carrier gas and free convection from the SDG housing to the ambient air. Using an input power of 2 W for the case of the pair of 2-mm Ni electrodes (i.e., using an input energy of 10 W and the estimated values of α as calculated above), we determine the temperature profile on the surface of the electrodes (cf. right subplot of Figure S9 in the SI), and a temperature value at the point of the thermocouple of ca. 363 K, which is very close to what we measured.

To determine the dependence of heat losses on the electrode diameter, we have to estimate how the temperature varies axially and radially, and more specifically the associated values at the two ends (i.e., the face temperature and the temperature on the mount side), for electrodes of different diameters. To achieve that, we carried out COMSOL calculations, similar to those described in the previous paragraph, decreasing the diameter of the electrodes from 14 to 0.2 mm (cf. Section S.6 in the SI for more details). In brief, assuming a constant input power, these simulations

provided a steady state temperature distribution not only of the electrodes having different diameters, but also of the entire SDG chamber. We should note here that because we had to assume that the heating area is 1 mm in diameter (a limitation posed by the meshing employed in COMSOL), these calculations should be considered as a first approximation of the temperature distribution of electrodes having different diameters.

Figure 4 provides results from the COMSOL simulations showing the temperature distributions across electrodes having diameters that range from 0.15 to 12 mm, together with the temperature differences $\Delta T_{conduction} = T_{front} - T_{back}$ (cf. Equation (9)) and $\Delta T_{convection} = T_s - T_{gas}$ (cf. Equation (10)), as functions of the electrode diameter. As observed, the ends of the thin electrodes exposed to the sparks are significantly hotter (T_{front}) than the ends attached to the SDG holders (T_{back}), which is always very near to room temperature. The value of T_{gas} is ~298 K, which is the mean gas temperature far from the cylindrical surface of the electrodes (cf. Figure S13 in the SI).

Using the temperature distribution determined by COMSOL, we then estimated the power lost *via* heat conduction to the solid parts of the SDG chamber and *via* forced convection by the carrier gas flow. In order to do that, we used again Equations (8)–(10). Note that the carrier gas temperature far from the electrode surface is always equal to room temperature as indicated by the calculations. Stationary temperatures (T_{front}, T_{back}, T_s and T_{gas}) used in Equations (9) and (10) are determined as average values by integrating across the respective surfaces of the electrodes; cf. Table S4 that provides the above-mentioned temperature values derived by COMSOL for all the different electrode diameters simulated.

Figure 5 shows heat loss rate values of P_{cond} and P_{conv} as a function of the electrode diameter, expressed as fractions of the total power provided by the SDG circuit. We should point out that for an input power of 10 W and assuming that $\alpha \approx \beta = 0.2$, the thinnest electrodes (i.e., 0.2 mm diameter) used in the simulations reach a temperature of ca. 1010 K at their top surface (as calculated by COMSOL). This temperature is high, but still lower compared to the melting point of Ni, which is realistic. The carrier gas, as expected, is only heated very close to the hot electrode surfaces, and at the outlet of the SDG chamber it practically reaches room temperature. The temperature of the bulk solid parts of the SDG becomes slightly higher (i.e., by 4–5 K) than the room temperature, which is also realistic according to our experience under such

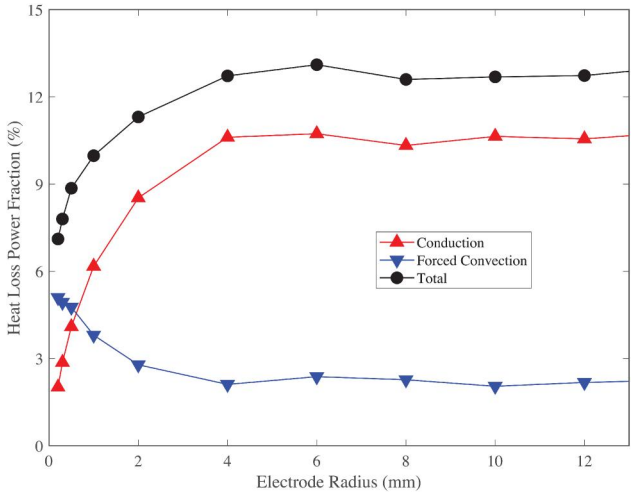

Figure 5. Fraction of input power lost as heat due to conduction and convection within the SDG chamber, determined by the COMSOL simulations.

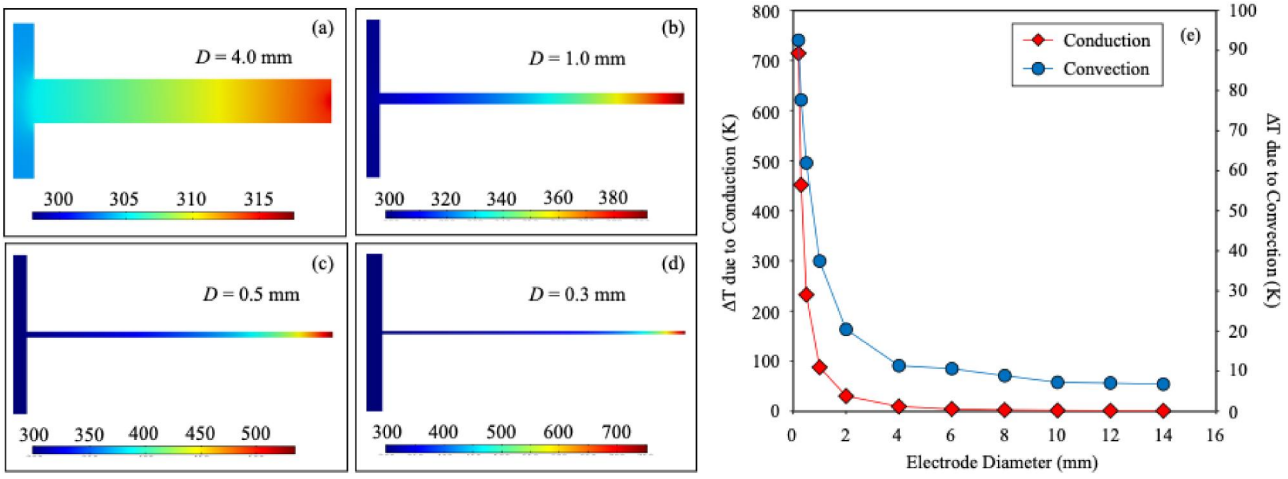

Figure 4. Temperature distributions along Ni electrodes of different diameters employed in the SDG, determined by the COMSOL simulations (a)–(d), and temperature deference between the front and back of the electrodes, or the carrier gas and the surface of the electrodes induced respectively by conduction or convection, as a function of the electrode diameter (e).

operating conditions (10 W total power). The whole SDG chamber, as mentioned above, is also cooled down externally by the ambient air *via* free convection, which explains why it is not overheated as the SDG operates continuously for a long time.

4.4. Effect of electric field focusing on ablation

The previous sections discussed how the thermal phenomena in SDGs can affect the ablation efficiency. Here we qualitatively point out a mechanism that may also have an influence when the electrode diameters are reduced. Apart from the decreased heat losses (parameter β), the ablation efficiency η, which is associated with an increase of nanoparticle throughput as discussed above, can increase due to the increase of the efficiency of energy transfer from the plasma to the electrodes, expressed by α in Equation (6). In fact, α can increase due to the focusing of the electric field between the bulk plasma and near the electrodes. To qualitatively understand this, we have to consider that the energy transfer from the spark plasma to the electrodes is mainly governed by the bombardment of the cathode by cations (Trodini, Richardson, and Schmidt-Ott 2019). This is in line with the observation that the cathode is more severely ablated, and that in an oscillatory discharge, which we typically have in SDGs, the electrodes take turns in acting as the cathode (Feng et al. 2018).

The cations are ionized gas atoms and molecules, while the negative charge carriers in the plasma are mainly electrons. The cations are accelerated toward the cathode by the strong electric field in a so-called thin "sheath zone" between the bulk of the plasma and the cathode surface as illustrated in Figure 6. Being much heavier than electrons they contribute more to the ablation. Due to the high concertation of electrons (compensated by positive ions for charge neutrality), the bulk of the spark plasma has a high electrical conductivity (Kohut et al. 2017), and consequently the voltage drop across it is small. So a considerable portion of the total voltage drop (in the order of hundreds of V) occurs in the sheath zone, which has an estimated thickness in the order of 100 nm (Trodini, Richardson, and Schmidt-Ott 2019), where the majority of cations reside and strongly accelerate leading to an energy exceeding 10 eV along their mean free path (~100 nm at normal pressure). Their impact with the cathode then heats the cathode face and releases surface atoms from the material.

We should stress here that electrode ablation is not driven by the electric field strength between the two electrodes (which serves to initiate the spark), but to the field created between the plasma and the cathode (to a larger extent) or the anode (to a smaller extent). The bulk plasma diameter is reported to be between 0.5 and 1.5 mm according to Palomares et al. (2015), under conditions comparable to the ones we used here (cf. Figure S14 in the SI). If the electrode tip diameter is smaller than the bulk plasma diameter as shown in Figure 6, the electric field must be focused in the vicinity of the cathode (cf. Figure 6b), so that the cations are accelerated to a higher kinetic energy near the cathode surface than in the case of electrodes that exceed the bulk plasma diameter.

This phenomenon can be regarded as an additional contribution to the field enhancement discussed above. Although extremely difficult to quantify, it is very well possible that this effect contributes to the higher efficiency of spark ablation of thin electrodes as compared to the thicker ones. While the total cation current within the sheath region is expected to be similar in both cases, the higher acceleration of the cations before they collide with the cathode and after their last collision with the gas molecules, makes the difference. Thus, a higher average energy is transferred to the cathode by each cation and less is transferred to the gas molecules within the sheath zone.

4.5. Semi-empirical model

The measurements in Figure 3 show that the ablation efficiency scales with electrode diameter as $\eta = c{\cdot}D^x$,

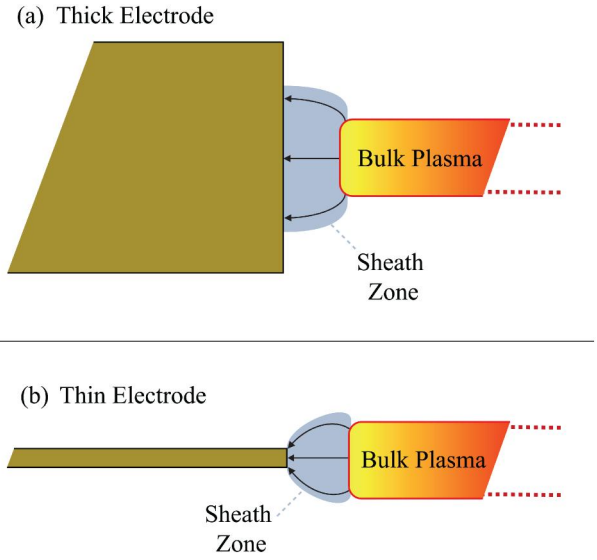

Figure 6. Illustration of electric field lines near the cathode for the cases where the diamter of the cathode electrode is larger (a) or smaller (b) than that of the bulk plasma. The region between the plasma and the electrodes is a sheath zone within which the ions are accelerated toward the cathode electrode.

where $c = 0.0921$ and $x = -0.834$ for Ni, $c = 0.0155$ and $x = -0.835$ for Cu, $c = 0.045$ and $x = -0.878$ for Pd. Considering the values of c and x in these fittings, the relation between ablation efficiency and electrode diameter can be approximated by the following power law:

$$\eta = \eta_0 \cdot \left(\frac{D}{D_0}\right)^{-1}, \tag{11}$$

where η_0 is the ablation efficiency determined experimentally for a specific electrode diameter D_0 for any given material. We should note here the inverse proportionality between the electrode diameter with the ablation efficiency, and consequently of the mass throughput of the process is consistent with the results reported by Domaschke, Schmidt, and Peukert (2018) who measured the mass concentration of particles produced spark-ablating Cu electrodes of different diameters and correlated these measurements with the diameter of the electrodes (cf. Section S.4 in the SI).

The nanoparticle mass production rate by spark ablation, $\dot{m}$, is a variable that can be used to describe the throughput of SDGs. Our results clearly show that the energy efficiency η of the process depends both on the material and the diameter of the electrodes employed in the SDG (cf. Figure 3). Previous work by Tabrizi et al. (2009), also shows that the gas has an influence on the mass production rate, which must also be connected in the energy needed for evaporation. Taking this two points together, Equation (11) can be extended to the following expression:

$$\eta = \eta_0 \cdot f_g \cdot \frac{D_0}{D}, \tag{12}$$

where f_g is a correction factor accounting for different carrier gases with values of unity for Ar and 0.38 for N_2 (Schmidt-Ott 2020).

Solving Equation (6) for η and substituting in Equation (12) we obtain:

$$\frac{\dot{m}_{mat}}{P_{tot}} = C_{mat} \cdot \eta_{0,mat} \cdot f_g \cdot \frac{D_{0,mat}}{D}, \tag{13}$$

where $C_{mat} = \frac{1}{\left(C_{ps}(T_m - T) + C_{pl}(T_b - T_m) + H_m + H_e\right)}$ is the inverse energy per unit mass required for evaporation of the electrode material, also referred to as the ablatability of the material, and $\eta_{0,mat}$ is the material-specific ablation efficiency corresponding to diameter $D_{0,mat}$ of the same material. Considering that values of $\eta_{0,mat}$ are not available for most materials, we rely on reported measurements of ablatability ratios, determined as the relative ablation rates of any given material with respect to that of Au (cf. Sect. S.9 in the SI), given by:

$$R_{abl} = \frac{\dot{m}_{mat}}{\dot{m}_{Au}} = \frac{C_{mat}}{C_{Au}} \cdot \frac{\eta_{0,mat}}{\eta_{0,Au}}, \tag{14}$$

Combining Equations (13) and (14) yields:

$$\dot{m}_{mat} = P_{tot} \cdot R_{abl} \cdot C_{Au} \cdot \eta_{0,Au} \cdot f_g \cdot \frac{D_{0,Au}}{D}, \tag{15}$$

or, considering that $C_{Au} \cdot \eta_{0,Au} = \dot{m}_{Au}/P_{tot,Au}$, we can write:

$$\dot{m} = \dot{m}_{Au} \cdot R_{abl} \cdot f_g \cdot \frac{P_{tot}}{P_{tot,Au}} \cdot \frac{D_{0,Au}}{D}, \tag{16}$$

where $\dot{m}_{Au} = 1.152$ mg/h is the mass production rate of Au electrodes, having a diameter $D_{0,Au} = 6.0$ mm, that are spark-ablated in N_2, leading to $f_g = 0.38$, when the $P_{tot,Au} = 8.4$ mJ. Figure 7 correlates ablation rate values (i.e., mass production rates) $\dot{m}_{mat}$ calculated by Equation (16) with values determined by the measurements using Ni, Pd, Cu, and Sn electrodes of different diameters. We should note here that there are systematic overestimated production rates in the results provided in Figure 7, that are associated to the thinnest (0.15 or 0.25 mm) Ni electrodes tested. This can be attributed to experimental uncertainties and errors associated to the fitting of Equation (11) to the measurements, which can yield an overestimation of a factor of 2 for these electrode diameters.

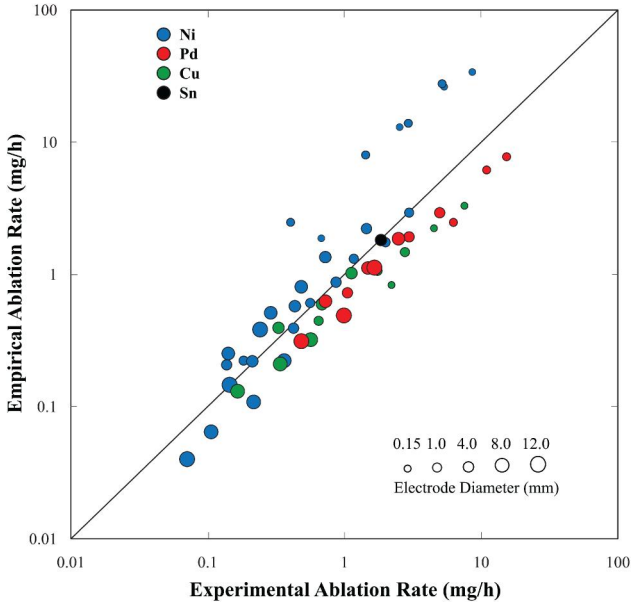

Figure 7. Correlation between the ablation efficiency determined by the experiments (values in the x axis) and by the simplified scaling law relating it with the diameter of the electrodes (values in the y axis) for all the materials tested in this work. The size of the circles indicates the diameter of the electrodes, ranging from 0.15 to 12 mm.

5. Conclusions

We provide quantitative and qualitative results showing why the throughput from the SDG increases as the electrode diameter decreases, and demonstrate that this effect is associated with a substantial increase of the ablation efficiency, η, (i.e., the energy spent to produce nanoparticles per unit of total input energy) as a result of decreased heat losses. We also show that the commonly used Llewellyn-Jones model for predicting the mass of nanoparticles produced by spark ablation cannot capture this effect, and thus we modify it to account for heat losses that become important when the electrode diameter is reduced below ca. 2 mm. This is achieved by defining the ablation efficiency as $\eta = \alpha - \beta$, where α is the fraction of the total input energy transferred to the electrodes and β the fraction of the total input energy lost as heat. Our measurements indicate that η is a small difference between two large quantities: α and β. The fraction of the total input energy transferred to the electrodes, α, is difficult to determine theoretically, as it depends on complex processes in and around the spark plasma. Showing that $\alpha \approx \beta$, however, we can approximate α α by determining β through temperature measurements of the hot surface of the electrodes. The resulting values of β are remarkably high, with the main energy losses being through thermal conduction of the electrodes, and, to a smaller degree, through gas convection.

Going a step further, and according to the updated model, an increase of the ablation efficiency, η, and consequently of the SDG throughput, could be achieved by further reducing the heat losses around the place where the ablation takes place; something that can be achieved if the electrodes consist of an electrically conductive material with low heat conductivity (cf. Equation (9) in Section 3). Following this train of thought, sintered metals or metal foams should achieve higher nanoparticle production rates, as long as Joule heating remains much smaller than the heat loss. We believe that considerable increases of the mass throughput should be achievable, as our results estimate the efficiency of energy transfer to the electrodes to be $\approx 20\%$, while typical energy efficiencies η are less than 0.1%.

An additional mechanism that may contribute to the increased mass throughput with decreasing electrode diameter is the focusing of the electric field in the so-called "sheath zone" of the spark plasma. When the electrode diameter becomes equal to or smaller than the bulk plasma diameter, the electric field near the electrode becomes stronger causing the cations to collide with the cathode having a higher average kinetic energy, and consequently leading to stronger ablation. Our measurements also show that the ablation efficiency scales with the inverse of the electrode diameter. Using this observation, and the updated Llewellyn-Jones model, we provide a semi-empirical equation that relates the mass production rate to the input power to the SDG, the ablatability ratios of the electrode material and its diameter.

Disclosure statement

No potential conflict of interest was reported by the author(s).

References

Domaschke, M., M. Schmidt, and W. Peukert. 2018. A model for the particle mass yield in the aerosol synthesis of ultrafine monometallic nanoparticles by spark ablation. *J. Aerosol Sci.* 126:133–42. doi: 10.1016/j.jaerosci.2018.09.004.

Efimov, A. A., A. A. Lizunova, I. A. Volkov, D. A. Mylnikov, P. V. Arsenov, and V. V. Ivanov. 2016. A new approach to the high-yield synthesis of nanoparticles by spark discharge. *J. Phys: Conf. Ser.* 741 (1):012035. doi: 10.1088/1742-6596/741/1/012035.

Efimov, A. A., V. V. Ivanov, A. V. Bagazeev, I. V. Beketov, I. A. Volkov, and S. V. Shcherbinin. 2013. Generation of aerosol nanoparticles by the multi-spark discharge generator. *Tech. Phys. Lett.* 39 (12):1053–6. doi: 10.1134/S1063785013120067.

Faghri, A., Y. Zhang, and J. R. Howell. 2010. *Advanced heat and mass transfer*. Columbia, MO: Global Digital Press.

Feng, J., G. Biskos, and A. Schmidt-Ott. 2015. Toward industrial scale synthesis of ultrapure singlet nanoparticles with controllable sizes in a continuous gas-phase process. *Sci. Rep.* 5 (1):15788. doi: 10.1038/srep15788.

Feng, J., N. Ramlawi, G. Biskos, and A. Schmidt-Ott. 2018. Internally mixed nanoparticles from oscillatory spark ablation between electrodes of different materials. *Aerosol Sci. Technol.* 52 (5):505–14. doi: 10.1080/02786826.2018.1427852.

Feng, J., X. Guo, N. Ramlawi, T. V. Pfeiffer, R. Geutjens, S. Basak, H. Nirschl, G. Biskos, H. W. Zandbergen, and A. Schmidt-Ott. 2016. Green manufacturing of metallic nanoparticles: A facile and universal approach to scaling up. *J. Mater. Chem. A* 4 (29):11222–7. doi: 10.1039/C6TA03221D.

Gutierrez, C. T., C. Loizides, I. Hafez, A. Brostrøm, H. Wolff, J. Szarek, T. Berthing, A. Mortensen, K. A. Jensen, M. Roursgaard, et al. 2023. Acute phase response following pulmonary exposure to soluble and insoluble metal oxide nanomaterials in mice. *Part. Fibre Toxicol.* 20 (1):4. doi: 10.1186/s12989-023-00514-0.

Han, K., W. Kim, J. Yu, J. Lee, H. Lee, C. Gyu Woo, and M. Choi. 2012. A study of pin-to-plate type spark discharge generator for producing unagglomerated

nanoaerosols. *J. Aerosol Sci.* 52:80–8. doi: 10.1016/j.jaerosci.2012.05.002.

Isaac, N. A., I. Pikaar, and G. Biskos. 2022. Metal oxide semiconducting nanomaterials for air quality gas sensors: Operating principles, performance, and synthesis techniques. *Mikrochim. Acta.* 189 (5):196. doi: 10.1007/s00604-022-05254-0.

Isaac, N. A., M. Valenti, A. Schmidt-Ott, and G. Biskos. 2016. Characterization of tungsten oxide thin films produced by spark ablation for NO2 gas sensing. *ACS Appl. Mater. Interfaces.* 8 (6):3933–9. doi: 10.1021/acsami.5b11078.

Ivanov, V. V., A. A. Efimov, D. A. Mylnikov, A. A. Lizunova, A. V. Bagazeev, I. V. Beketov, and S. V. Shcherbinin. 2016. High-efficiency synthesis of nanoparticles in a repetitive multigap spark discharge generator. *Tech. Phys. Lett.* 42 (8):876–8. doi: 10.1134/S1063785016080023X.

Kohut, A., G. Galbács, Z. Márton, and Z. Geretovszky. 2017. Characterization of a copper spark discharge plasma in argon atmosphere used for nanoparticle generation. *Plasma Sources Sci. Technol.* 26 (4):045001. doi: 10.1088/1361-6595/aa5c2b.

Llewellyn Jones, F. 1950. Electrode erosion by spark discharges. *Br. J. Appl. Phys.* 1 (3):60–5. doi: 10.1088/0508-3443/1/3/302.

Lu, J., J. Guo, S. Song, G. Yu, H. Liu, X. Yang, and Z. Lu. 2020. Preparation of Ag nanoparticles by spark ablation in gas as catalysts for electrocatalytic hydrogen production. *RSC Adv.* 10 (63):38583–7. doi: 10.1039/D0RA06682F.

Maisser, A., K. Barmpounis, M. B. Attoui, G. Biskos, and A. Schmidt-Ott. 2015. Atomic cluster generation with an atmospheric pressure spark discharge generator. *Aerosol Sci. Technol.* 49 (10):886–94. doi: 10.1080/02786826.2015.1080812.

Maisser, A., K. Barmpounis, S. Holm, M. Attoui, A. Schmidt-Ott, J. Kangasluoma, and G. Biskos. 2021. Characterization of atmospheric-pressure spark generated atomic silver and gold clusters by time-of-flight mass spectrometry. *J. Aerosol Sci.* 156:105780. doi: 10.1016/j.jaerosci.2021.105780.

Messing, M. E., R. Westerström, B. O. Meuller, S. Blomberg, J. Gustafson, J. N. Andersen, E. Lundgren, R. van Rijn, O. Balmes, H. Bluhm, et al. 2010. Generation of Pd model catalyst nanoparticles by spark discharge. *J. Phys. Chem. C* 114 (20):9257–63. doi: 10.1021/jp101390a.

Minogiannis, P., M. Valenti, V. Kati, O.-I. Kalantzi, and G. Biskos. 2019. Toxicity of pure silver nanoparticles produced by spark ablation on the aquatic plant Lemna minor. *J. Aerosol Sci.* 128:17–21. doi: 10.1016/j.jaerosci.2018.11.003.

Noh, S. R., D. Lee, S. J. Park, D. S. Kim, and M. Choi. 2017. High throughput nanoparticle generation utilizing high-frequency spark discharges via rapid spark plasma removal. *Aerosol Sci. Technol.* 51 (1):116–22. doi: 10.1080/02786826.2016.1239814.

Palomares, J. M., A. Kohut, G. Galbács, R. Engeln, and Z. Geretovszky. 2015. A time-resolved imaging and electrical study on a high current atmospheric pressure spark discharge. *J. Appl. Phys* 118 (23):233305. doi: 10.1063/1.4937729.

Petallidou, K. C., P. Ternero, M. E. Messing, A. Schmidt-Ott, and G. Biskos. 2023. Tuning atomic-scale mixing of nanoparticles produced by atmospheric-pressure spark ablation. *Nanoscale Adv.* 5 (24):6880–6. doi: 10.1039/D3NA00152K.

Petallidou, K., A. Schmidt-Ott, and G. Biskos. 2024. Stability of nanoparticle production by atmospheric-pressure spark ablation. *Aerosol Sci. Technol.* 58 (9):1079–88. doi: 10.1080/02786826.2024.2347999.

Pfeiffer, T. V., J. Feng, and A. Schmidt-Ott. 2014. New developments in spark production of nanoparticles. *Adv. Powder Technol.* 25 (1):56–70. doi: 10.1016/j.apt.2013.12.005.

Schmidt-Ott, A, ed. 2020. *Building Blocks for Nanotechnology*. New York: Jenny Stanford Publishing.

Schwyn, S., E. Garwin, and A. Schmidt-Ott. 1988. Aerosol generation by spark discharge. *J. Aerosol Sci.* 19 (5):639–42. doi: 10.1016/0021-8502(88)90215-7.

Tabrizi, N. S., M. Ullmann, V. A. Vons, U. Lafont, and A. Schmidt-Ott. 2009. Generation of nanoparticles by spark discharge. *J. Nanopart. Res.* 11 (2):315–32. doi: 10.1007/s11051-008-9407-y.

Trodini, E., I. M. Richardson, and A. Schmidt-Ott. 2019. The Physics and Equivalent Circuit Modeling of Spark Ablation. In *Spark Ablation*, ed. A.Schmidt-Ott. New York: Jenny Stanford Publishing.

Zhang, S.-H., Y. Akutsu, L. M. Russell, R. C. Flagan, and J. H. Seinfeld. 1995. Radial Differential Mobility Analyzer. *Aerosol Sci. Technol.* 23 (3):357–72. doi: 10.1080/02786829508965320.